Shear-wave velocity imaging of weathered granite in La Campana (Chile) from Bayesian inversion of micro-tremor H/V spectral ratios

Rahmantara Trichandi [a,b,*], Klaus Bauer [a], Trond Ryberg [a], Britta Wawerzinek [a], Jaime Araya Vargas [c], Friedhelm von Blanckenburg [a,d], Charlotte M. Krawczyk [a,b]

[a] GFZ German Research Centre for Geosciences, Telegrafenberg, 14473 Potsdam, Germany
[b] Technische Universität Berlin, Ernst-Reuter-Platz 1, 10587 Berlin, Germany
[c] Departamento de Geología, Universidad de Atacama, Copiapó, Chile
[d] Institute of Geological Sciences, Freie Universität Berlin, Berlin, Germany

ABSTRACT

Subsurface imaging of the regolith layer is an important tool for weathering zone characterization. For example, the extent of bedrock modification by weathering processes can be modelled by means of differing seismic velocities. We acquired a 360 m-long seismic profile in central Chile to characterise weathering at a semi-arid site. We used 87 3-component geophones, which continuously recorded ambient seismic noise for three days. The seismic line was centered at an 88 m deep borehole, providing core and downhole logging data for calibration. We extract Horizontal-to-Vertical Spectral Ratio (HVSR) curves along the seismic line to image the subsurface. Temporal analysis of the HVSR curves shows that the ambient noise vibrations recorded during the nighttime provide more stable HVSR curves. The trans-dimensional Bayesian Markov chain Monte Carlo (McMC) approach was used to invert the micro-tremor HVSR curves at each station to reconstruct 1D shear-wave velocity (Vs) models. The resulting individual 1D Vs models were merged to create a 2D Vs model along the linear seismic array in La Campana. The resulting Vs model shows an increase from 0.85 km/s at the surface to ca. 2.5 km/s at 100 m depth. We use the interface probability as a by-product of the Bayesian inversion to apply a more data-driven approach in identifying the different weathering layers. This method identified the boundary between saprolite and fractured bedrock at 42 m depth at the borehole, as evidenced by the interpretation of downhole logging data such as magnetic susceptibility. The resulting 2D Vs model of this site in Mediterranean climate shows a strong correlation between the interpreted weathering front at around 90-m depth and a higher precipitation rate in the study site compared to arid sites. The horizontal alignment of the weathering front indicates a correlation between the weathering front depth with topography and fractures in the bedrock.

1. Introduction

Advances in geophysical methods provide tools for imaging of the subsurface weathering structures. Various geophysical imaging techniques, including electrical resistivity tomography (Holbrook et al., 2014; Olona et al., 2010), Ground Penetrating Radar (GPR) (Dal Bo et al., 2019) and seismic tomography (Befus et al., 2011; Handoyo et al., 2022; Olona et al., 2010; Trichandi et al., 2022) have been extensively used to study the weathering zone due to their capabilities to produce 2D/3D subsurface images. Further experience is gained by near-surface surveying, for instance, in karstic regions and sinkhole areas (Al-Halbouni et al., 2021; Krawczyk et al., 2012; Wadas et al., 2020). These non-

invasive approaches do not disturb the subsurface structure and cost less than drilling multiple boreholes in the same area.

Seismic imaging is one of the most common geophysical methods used in weathering zone investigation (Befus et al., 2011; Flinchum et al., 2018; Olona et al., 2010; Trichandi et al., 2022). Elastic seismic properties such as P-wave velocity (Vp) and S-wave velocity (Vs) can be estimated by analysis and inversion of body waves and surface waves. Using seismic active sources such as weight drop and vibroseis, seismic waves are excited to the subsurface and are recorded by seismic receiver arrays. However, data acquisition of such controlled-source experiments often requires extensive equipment with associated logistical challenges in remote or inaccessible study sites. Additionally, high-impact seismic

sources are often restricted in conservation areas such as national parks or nature reserves.

The micro-tremor Horizontal-to-Vertical Spectral Ratio (HVSR) technique is a passive seismic method that does not require active seismic sources (Arai and Tokimatsu, 2004; Mucciarelli and Gallipoli, 2001). This method is still the most used for the study of site response for seismic hazard evaluation (Cultrera et al., 2021; Mahajan et al., 2012; Nardone et al., 2023; Piña-Flores et al., 2020) and the imaging of sediment basins (e.g. Cipta et al., 2018; Koesuma et al., 2017; Pastén et al., 2016; Pilz et al., 2010). Recently, the method has been used at smaller scales for bedrock investigation (Maghami et al., 2021; Moon et al., 2019; Nelson and McBride, 2019) due to the simplicity and speed of the data acquisition, as well as the ease of acquisition point placement. The HVSR method has emerged as a cost-effective method to produce a reliable subsurface image of the weathering zone. However, the solution to the inverse problem of the HVSR curve is highly non-unique and thus requires prior information of the subsurface structure (Moon et al.,

2019; Nelson and McBride, 2019; Pilz et al., 2010). Additional data such as the phase velocity dispersion curve of surface waves (e.g., Arai and Tokimatsu, 2005; Scherbaum et al., 2003) or the micro-tremor HVSR measurements at depth (Lontsi et al., 2015; Spica et al., 2018) are also used to constrain the inversion results.

The trans-dimensional and hierarchical Bayesian McMC approach can help resolve the prior information required for model initiation in the HVSR curve inversion. The Bayesian McMC inversion routine needs only minimum prior information on the subsurface structure (Ryberg and Haberland, 2019; Trichandi et al., 2022). Furthermore, the trans-dimensional approach enables changes in dimensionality during the inversion process, so we can avoid the need for prior constraints on defining the number of layers (Bodin, 2010; Bodin et al., 2012; Cipta et al., 2018). This procedure also decreases uncertainty and provides a robust, data-driven Vs model to be interpreted.

In this paper, we discuss the inversion of HVSR curves data using the trans-dimensional and hierarchical Bayesian inversion approach to
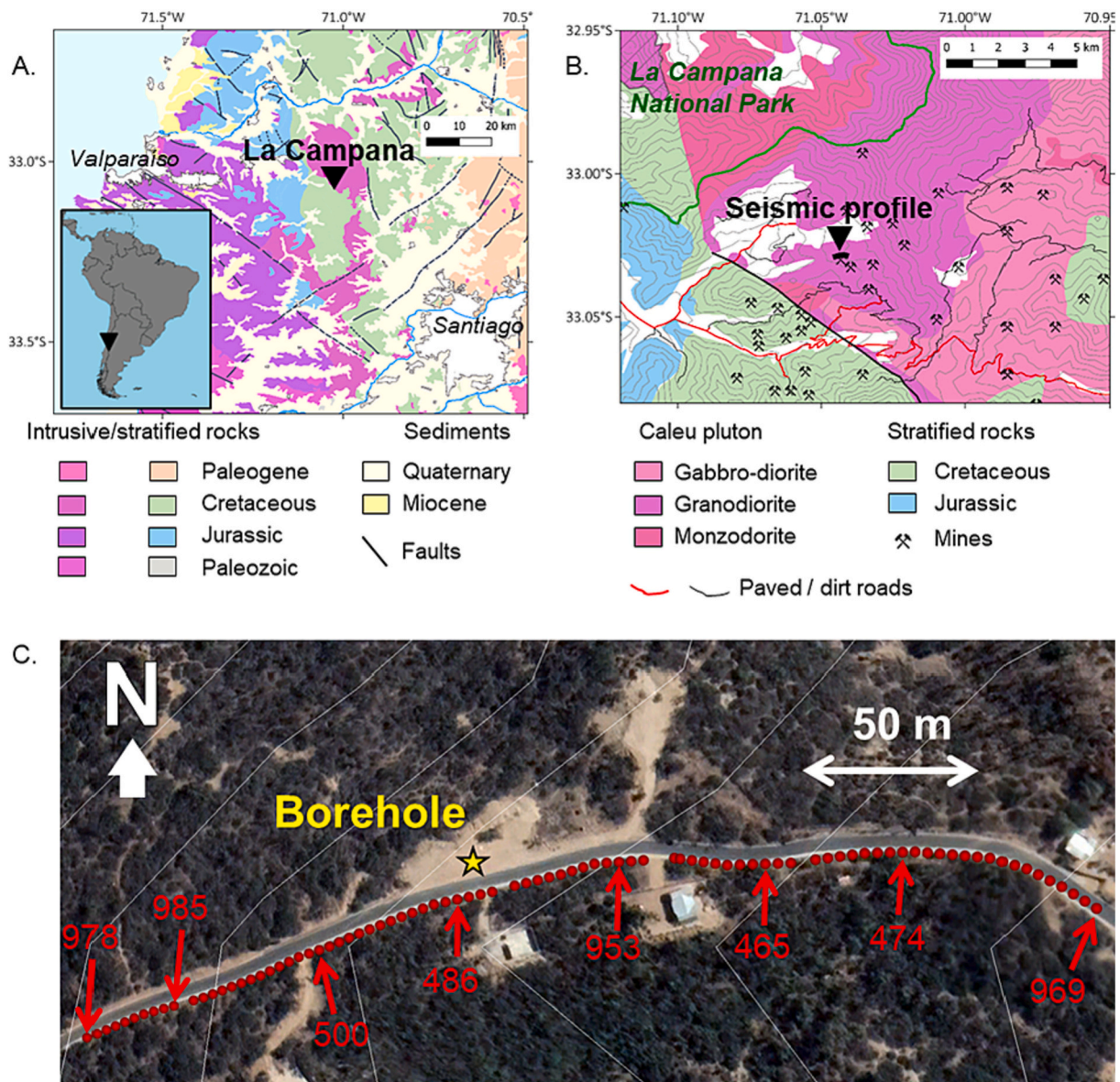

Fig. 1. Geology at the La Campana study site in Chile: (A) Location and regional geological setting of the study area (Modified from Sernageomin, 2003). (B) Local geological map with the location of the seismic profile and borehole location (Modified from Gana et al. (1996), Parada et al. (2005), and Molina et al. (2015)) with topographic contour every 100 m elevation. (C) Seismic station geometry (red dot) and the borehole location (yellow star) with topographic contour every 10 m elevation. (For interpretation of the references to colour in this figure legend, the reader is referred to the web version of this article.)

image the weathering fronts in the Mediterranean climate zone of the EarthShape (Earth Surface Shaping by Biota) project, which aims to study weathering processes in different climate zones (Oeser et al., 2018; Oeser and Von Blanckenburg, 2020). The site is located in the Coastal Mountains of Chile, south of the La Campana National Park, one of the four major Earthshape study sites. With the La Campana study presented herein, we tested the hypothesis that higher precipitation rates affect the depth of the weathering front.

2. Study site and geologic setting

The study site (−33.02833° N, −71.04354° E, 898 m) is located in the Coastal Cordillera 60 km north-west of Santiago de Chile (Fig. 1A) on a ridge with flanks dipping steeply with 20–30°, in a semi-arid/ Mediterranean climate with vegetation of a Mediterranean scle-rophyllous forest with inter-dispersed shrubs (Arroyo et al., 1993; Oeser et al., 2018). The mean annual precipitation in the area is 326 mm/year, with a mean annual temperature of 14.9 °C (Karger et al., 2017). Pre-vious research has shown that the average soil thickness in this area ranges between 0.40 and 0.60 m (Bernhard et al., 2018; Oeser et al., 2018). Additionally, subsurface investigation with the Ground Pene-trating Radar (GPR) method managed to image the shallow subsurface down to 2.5 m depth with high resolution above the saprolite (Dal Bo et al., 2019). However, the resulting GPR imaging could not reach the bedrock layer. A study site at Curacavi (approximately 50 km south of La Campana), an adjacent area in the coastal mountains, revealed a saprolite layer exceeding 30 m thick (Vázquez et al., 2016), which suggests a deep weathering zone in our study area as well.

The La Campana seismic study site is located in a granodiorite unit of the Early Cretaceous Caleu pluton (Molina et al., 2015; Parada et al., 2005; Fig. 1B). U—Pb and Ar/Ar dates suggest that the Caleu pluton was emplaced ca. 93–97 Ma (Molina et al., 2015; Parada et al., 2005). This granodiorite unit comprises biotite, amphibole, and minor pyroxene granodiorites (Molina et al., 2015). The presence of small mines with vein-type mineralization around the study site, as well as the proximity to the contact (< 3 km distance) between the Caleu pluton and Lower Cretaceous sedimentary and volcanic rocks, suggest that lithological heterogeneities can be found in the bedrock below the seismic profile. In 2020, a drilling campaign was conducted to explore the weathering zone. The borehole cuts a fine-grained granodiorite with plagioclase, quartz, microcline, hornblende, biotite, and abundant chlorite (~5% of total weight) replacing biotite (Hampl et al., 2023). The rock also shows minor magnetite (~0.9% of total volume) and traces of pyrite and chalcopyrite (Hampl et al., 2023).

3. Data acquisition

We acquired passive seismic data in La Campana in November 2019 along a 360-m-long profile that transects a borehole location (Fig. 1C). Elevation along the profile varies between 877 and 926 m. The passive seismic data was acquired using 87 3-component (3-C) geophones with 4.5 Eigenfrequency (PE-6/B by SENSOR Nederland). While the geo-phones have a relatively limited frequency sensitivity in the lower fre-quency range, based on modelling tests, we consider the given frequency content sufficient as we are interested in the shallow subsurface. The geophones were planted firmly along the profile to ensure sufficient coupling to the ground. Each geophone was connected to a CUBE data logger (DATA-CUBE³ Type 1 (int) – by DiGOS), which records the seismic vibrations detected by the geophones with 400 Hz sampling frequency. The geophones were distributed along the profile with 4 m spacing in between. Using this setup, we acquired three days of ambient seismic noise data, which we used for the spectral ratio analysis.

At the center of the seismic profile (close to station 486), an 88-m-deep borehole was drilled to recover core material and conduct geophysical downhole logging. Different groups and disciplines pres-ently analyse the core material, including petrology, geochemistry, and

microbiology (e.g., Hampl et al., 2023). In this paper, we use selected downhole logs to support the interpretation of the seismic imaging re-sults, especially Gamma Ray and magnetic susceptibility (Fig. 2).

4. Methodology

To produce a subsurface image of the profile using the Horizontal-to-Vertical Spectral Ratio (HVSR) method, we first need to extract the HVSR curve from the passive seismic data. We produce the HVSR curve for each station using a statistical approach (Vantassel, 2020), which also fulfills the SESAME guideline for site characterization (SESAME, 2004). We increase the quality of the extracted curves by performing a temporal analysis of the ambient noise data and selecting only the time windows that provide smaller data errors. The extracted curves are then individually inverted with a trans-dimensional, hierarchical Bayesian inversion approach to get the 1D Vs profile. With the multiple 1D Vs profiles, we compiled a pseudo-2D Vs section along the seismic line.

4.1. HVSR curve extraction

For HVSR curve extraction, we used the hvsrpy package (Vantassel, 2020). We first instrumentally correct and filter the data using a 1.0 to 150 Hz bandpass filter. This filter was applied to all three components of the data. We used three days of ambient micro-tremor data to extract the HVSR curve of each station location. We present an example of how we process a 60-min time window in Fig. 3. Fig. 3A–C shows a 60-min segment of all three seismic components: vertical, east-west, and north-south. The time series data were then transformed to the fre-quency domain with a straightforward Fourier transform, which
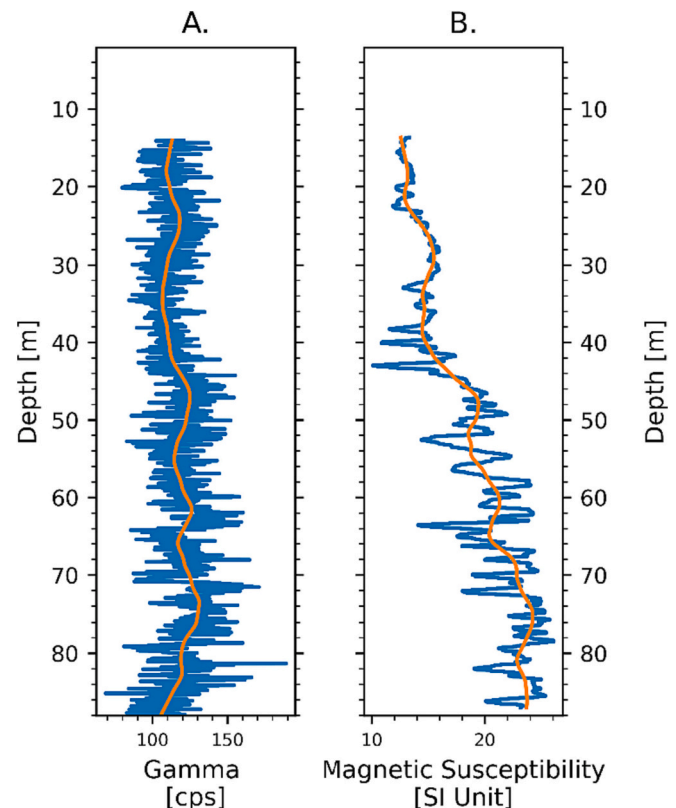

**Fig. 2.** Downhole geophysical logging performed from an existing borehole: total Gamma Ray (A) and magnetic susceptibility log (B). No data was obtained in the upper 14 m where the borehole was cased. Blue lines represent the high-frequency logging data, while the orange lines represent the smoothed data. (For interpretation of the references to colour in this figure legend, the reader is referred to the web version of this article.)
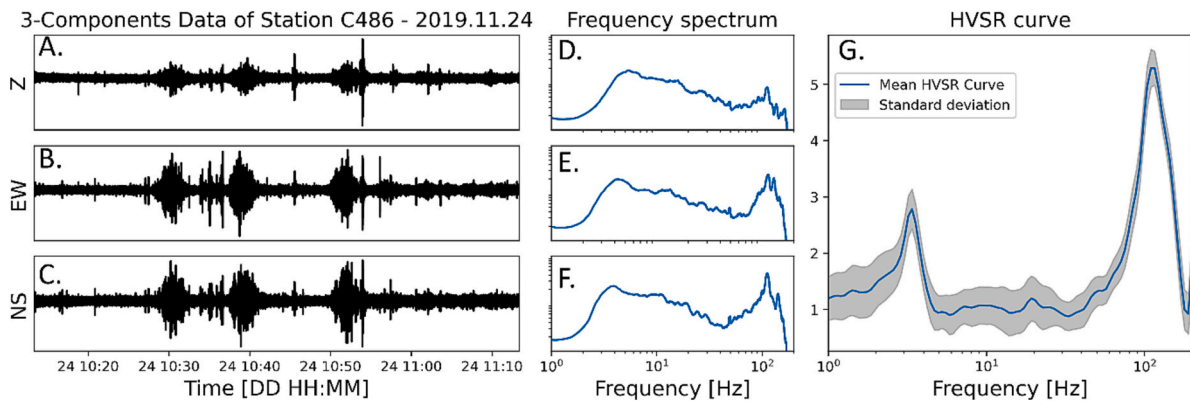
Fig. 3. Example of a 60-min segment of the acquired ambient seismic noise in the time domain from 3-component seismic recordings. (A) vertical, (B) east-west, (C) north-south direction, and their respective frequency spectra (D, E, F). (G) shows the extracted HVSR curve using the hvsrpy package (Vantassel, 2020) of the 1-h time window in (A)–(C).

provided the frequency spectrum data (Fig. 3D–F). We then followed the workflow of HVSR curve extraction as described by Cox et al. (2021), which rejects time windows that exceed a defined statistical threshold of the peak frequency (f_0) and HVSR curve variance. For this approach, the time series data was cut into 60-s time windows. This results in 60 HVSR curves for 60 min of data. The resulting mean HVSR curve (Fig. 3G) is finally derived by averaging the accepted HVSR curves in the 60-min window. This process also allows us to compute the standard deviation of the HVSR curve and assess the stability of the HVSR curve during this time window.

Assessing the stability of the HVSR curves is an important step to select/obtain an inversion target that is the best representative of the subsurface structure under investigation (e.g., Lontsi et al., 2023). To further increase the stability of the HVSR curve, we analyse the spectral variability of the recorded ambient seismic noise for different times of the day (Fig. 4). We inspected two different periods of recording time during daytime and nighttime and selected data from 07.00 h until 20.00 h as the daytime data and from 20.00 to 07.00 h as nighttime data. In daytime data (Fig. 4A, orange line), we observe several high-amplitude activities that could be related to human activities or other incoherent seismic noise. In contrast, the data during nighttime show only a few seismic events and are dominated by ambient seismic noise (Fig. 4A, blue line). The difference between daytime and nighttime data is more pronounced in the spectral ratio curves. During nighttime, the mean standard deviation of the HVSR curve (Fig. 4B) is relatively low

compared to daytime (Fig. 4C). The peak at a lower frequency (< 10 Hz) is much more pronounced when only using the nighttime data.

To further analyse the difference in HVSR curve stability during daytime and nighttime, we calculate the hourly mean, standard deviation of the HVSR curve (Fig. 4D). The hourly HVSR curve obtained during the day has a higher mean standard deviation, while the hourly analysed data during nighttime show significantly lower mean standard deviations. For this reason, we only use data recorded between 20.00 h and 07.00 h to extract the HVSR curve for each seismic station (We provided further examples of this temporal analysis from different stations in the supplementary material).

The consistency check of the peaks for all seismic stations reveals two frequency ranges with especially high amplitude in the lower frequency (< 10 Hz) and in the higher frequency (> 30 Hz) bands (Fig. 5A). The observed amplitude peaks at lower frequencies are also relatively consistent and are identifiable for all the recording stations. However, the high standard deviation shows that the high-frequency peaks are less consistent than the lower-frequency peaks. For this reason, we limit the HVSR curve input for the inversion to the lower frequency band (< 30 Hz). Nevertheless, we consider the frequency content to be sufficient in the context of weathering front imaging, as the lower frequency peak is often associated with the boundary between bedrock and regolith (Fig. 5B), while the higher frequency peak is more related to the shallower boundary between saprolite and soil (Nelson and McBride, 2019).
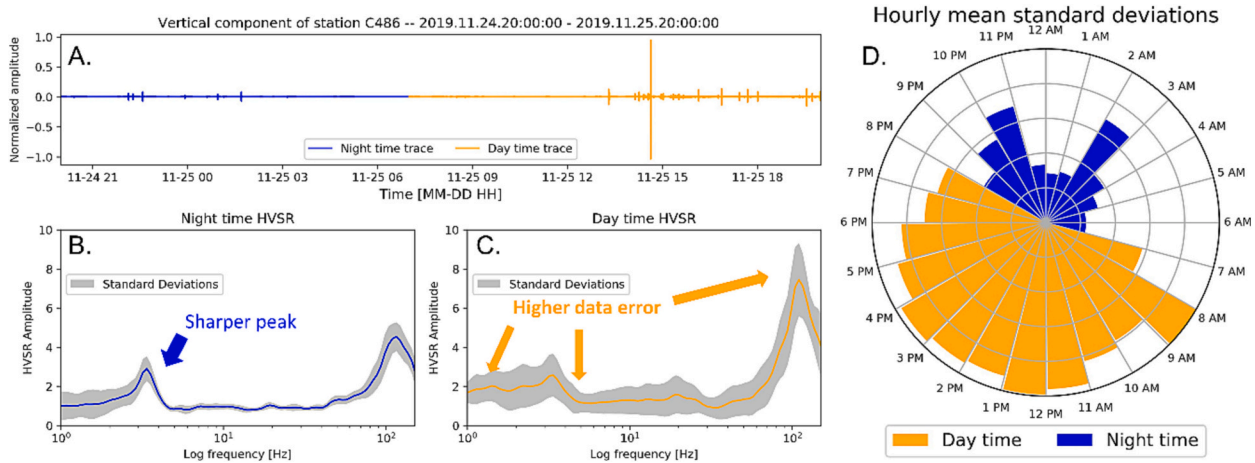
Fig. 4. Spectral variability analysis of the daytime (orange) and nighttime (blue) data examples (A) result in different HVSR curves (B and C). Hourly mean standard deviations and the used time window (D) reveal higher data quality during night time. (For interpretation of the references to colour in this figure legend, the reader is referred to the web version of this article.)
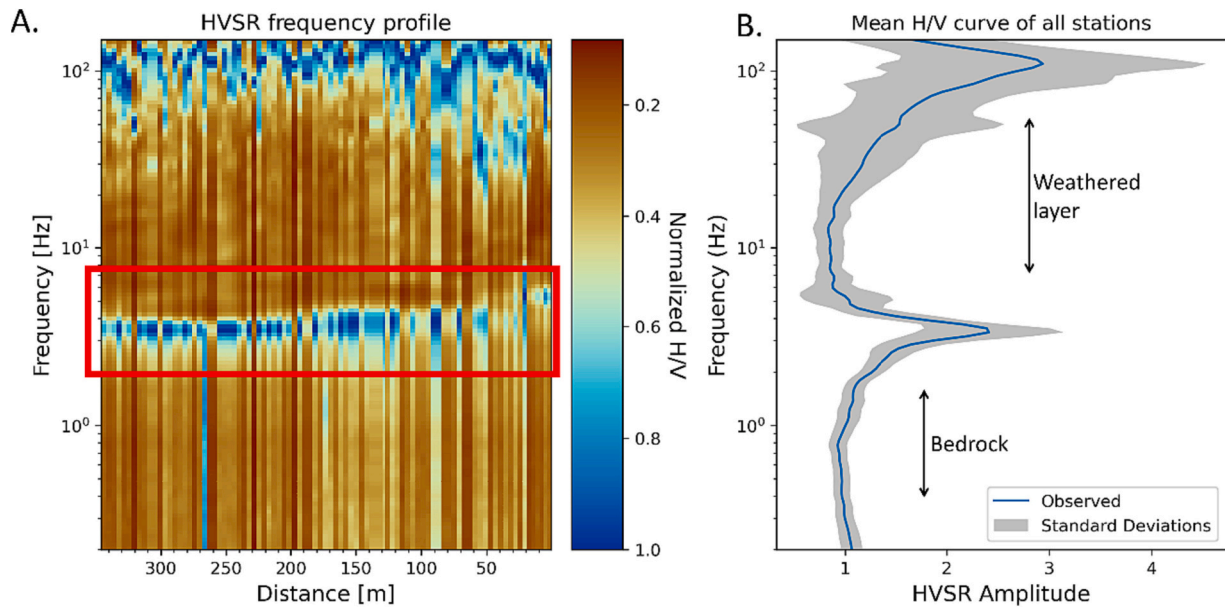
Fig. 5. Compilations of the HVSR curve along the profile distance (A) and the resulting mean HVSR curve (B). The red box in (A) highlights the low-frequency peak (< 10 Hz) in the HVSR curve along the profile. The mean HVSR curve in (B) shows two prominent frequency peaks in different frequency ranges. (For interpretation of the references to colour in this figure legend, the reader is referred to the web version of this article.)

4.2. HVSR curve inversion

Earlier investigations have established a strong relationship between the HVSR curve and the ellipticity of Rayleigh waves (Fäh et al., 2001; Lachet and Bard, 1994; Lermo and Chávez-García, 1993). In the process of inversion, our initial assumption is that the ambient seismic noise field is predominantly influenced by the fundamental mode of the Rayleigh wave, primarily due to its proximity to the ocean (Bonnefoy-Claudet et al., 2006). This implies that the primary sources of seismic noise are likely associated with Rayleigh waves excited by ocean swell (Longuet-Higgins, 1950; Yamanaka et al., 1993). Our HVSR curves also show a clear peak (f_0) attributed to the noise wavefield constituted dominantly by the fundamental mode of Rayleigh wave (Stephenson, 2003). Therefore, the prominent peak observed at frequencies below 10 Hz is highly probable to originate from this natural source of Rayleigh wave energy, particularly since our measurements were conducted during night time and their stability was verified. The observed curve also shows good temporal (Fig. 4B) and spatial (Fig. 5) stability of the fundamental frequency (f_0) (SESAME, 2004).

Assuming a 1D structure under a station, the HVSR curve can be used to reconstruct a 1D Vs model at the station's location. Introductions of constraints during the inversion process can help in addressing this non-uniqueness problem, including the usage of dispersion curves (Arai and Tokimatsu, 2004; Scherbaum et al., 2003), fixing the number of layers using known geological information (Fäh et al., 2003; Hobiger et al., 2013; Parolai et al., 2005; Wathelet et al., 2004), and fixing bedrock velocity (Parolai et al., 2005). These approaches simplify the inverse problem by providing prior information of the real model to the inversion scheme. In weathering zone investigations, for example, determining the expected number of layers is often not possible without previous subsurface investigation. Regarding fixing bedrock velocity, although we can have prior information on the velocity from previous research in similar bedrock, it is often that the velocity of the bedrock differs between different sites. Additionally, reliably fixing the bedrock velocity will require a petrophysical rock sample analysis.

For the parameterization in this study, we predefined a corridor of values to the inversion routine. We provide prior information on Vs value between 0.1 and 5.0 km/s. The low Vs estimate of 0.1 km/s was given to accommodate possible highly weathered layers such as soil and saprolite in the model. On the other hand, while Vs for a granitic bedrock that hardly reaches up to 4.0 km/s, we provide a high estimate of 5.0 km/s to accommodate any possible presence of other lithology in the subsurface and also to give the inversion more freedom to explore the model space. The prior information for the number of layers is uniform between 2 and 20 layers (including half space). While the structure of weathering layers is usually subdivided into 3 or 4 layers, we provide a low number of 2 layers to enable a relatively simple model created during the inversion routine. For example, it is possible only to have fractured bedrock and bedrock layers in an area with a relatively low weathering degree. Additionally, the simplified model can also integrate models with high data uncertainty. On the contrary, we allow for a maximum of 20 layers to accommodate the possibility of highly complex subsurface layering. The following parameters to be defined are Vp and density. Both parameters have been shown to have a significantly low sensitivity to the HVSR curve modelling and can be treated as unknown nuisances during the inversion (Cipta et al., 2018). Nevertheless, we also provide uniform corridors/range of Vp between 0.3 and 8.0 km/s and for density between 1.5 and 3.0 g/cm^3, respectively.

We initiate 24 parallel chains with 100,000 iterations for each chain per station. In each chain, the inversion routine starts with the initial model (m_0) generation drawn from the given uniform prior information of the parameters. We then perform a forward calculation of the model ($dcal_0$) using the Rayleigh wave ellipticity modelling module from the GEOPSY package (Wathelet et al., 2020). The forward calculation tool modelled the subsurface as homogeneous layers over a half-space. In defining the layered model, we used a 1D Voronoi cells (cells of equal distance) approach and calculated the thickness of each cell's layer. For every iteration, we perform one of the following perturbations:

a. Perturb the data noise (σ) value according to the proposal distribution.
b. Perturb the cell location of a random cell according to the proposal distribution. Changes in the Voronoi cell location will affect the layer's thickness of the input model.
c. Perturb the Vs value of a random cell according to the proposal distribution.
d. According to the proposal distribution, perturb a random cell's Vp/Vs value and calculate Vp accordingly for the input model.

e. Delete one random cell.
f. Add one random cell according to the prior information provided by the chain.

The perturbation generates a new model (m_1) for which we then calculate the theoretical HVSR curve ($dcal_1$). We then calculate the acceptance probability of moving from m_0 to m_1 based on d_{obs}, $dcal_0$, and $dcal_1$. We then randomly accept the move from m0 to m1 using the acceptance probability. If the move is accepted, m_1 will become m_0, and we continue to the next iteration. Otherwise, we keep m_0 and continue to the next iteration. The process is repeated until the predetermined iteration is reached. The final model for each station is derived by averaging all accepted models from all the chains performed (Bodin, 2010; Cipta et al., 2018; Ryberg and Haberland, 2019).

The subsurface Vs structure often emerged as a smooth function with depth. For example, the study in Santa Gracia National Park, Chile, which also studied the weathering zone using surface waves, shows a smooth Vs profile with depth instead of a sharp boundary (Trichandi et al., 2022). A synthetic model recovery test is performed to test the ability of our inversion scheme to resolve a smooth model (Fig. 6). We first defined a smooth Vs model shown as a red line in Fig. 6B and C. The smooth model was subdivided into a one-meter thick layer with gradually increasing Vs between a depth of 20 and 40 m. We then performed a forward calculation to produce the synthetic HVSR curve (Fig. 6A, orange line) and added random noise to the HVSR curve (Fig. 6, blue line).
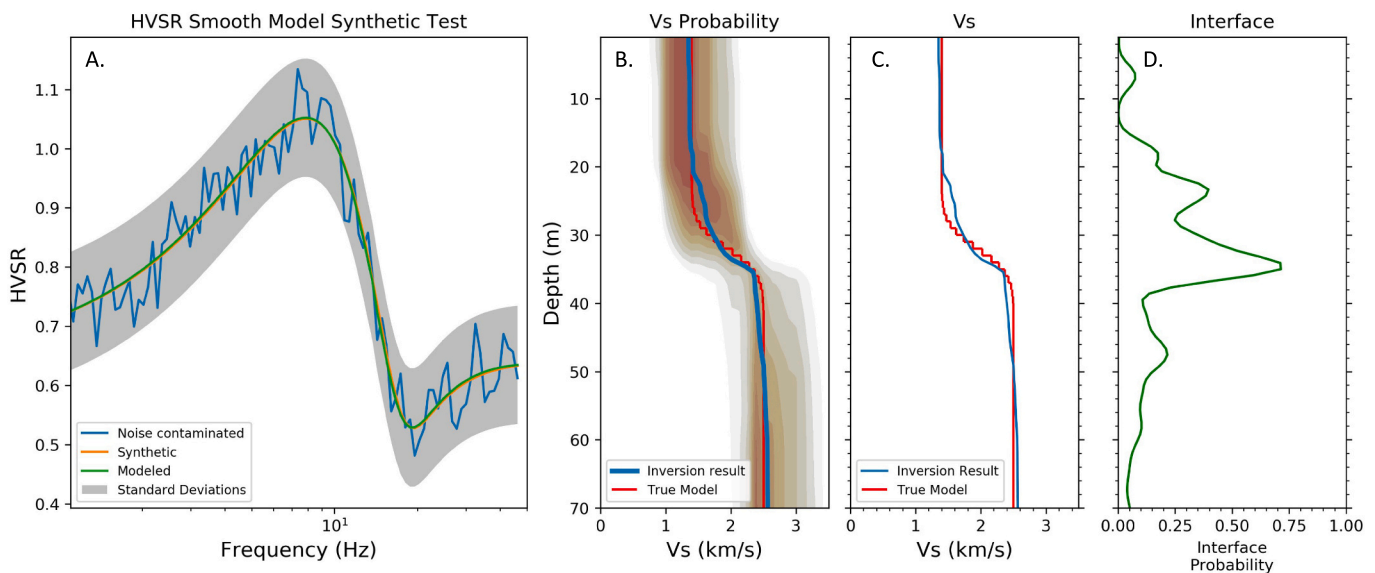
The noise-contaminated HVSR curve then goes through the inversion scheme. We recovered the synthetic HVSR curve nicely (Fig. 6A, green line) with acceptable model standard deviations (Fig. 6, grey area). The resulting Vs model (Fig. 6B and C, blue line) also matched nicely with the true model (Fig. 6B and C, red line). In Fig. 6B, we present a Vs – depth model space heatmap to show how the inversion scheme sampled the Vs – depth model space. Since the layer's thickness in our inversion scheme was not fixed, we also get an interface probability function from all the Vs models (Fig. 6D). The interface probability function represents a probability of possible layer change in the model. The presented synthetic model shows two prominent peaks at depths of around 20 and 40 m, where the smooth transition zone started and ended.
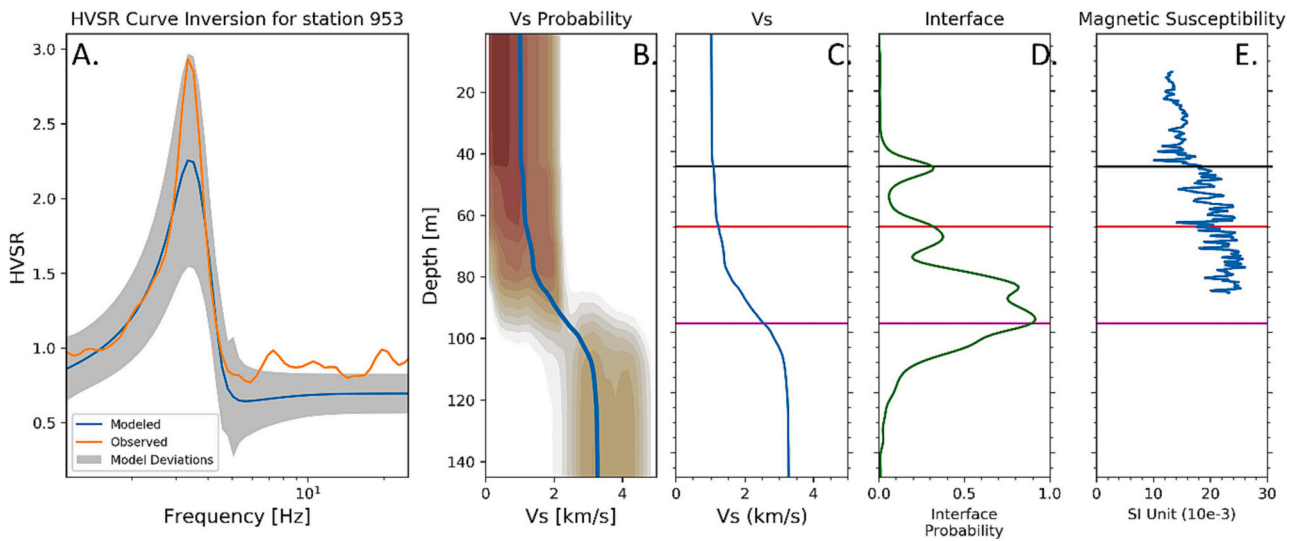
5. Results

The inversion for the La Campana data is shown in detail for the seismic station closest to the borehole location (Fig. 7). The observed and modelled HVSR curves match well for frequencies below 10 Hz and within the model standard deviation range (Fig. 7A). The inversion routine explores the model space from surface to depth, as shown by the Vs probability density value (Fig. 7B), resulting in the 1D Vs model (Fig. 7C). In Fig. 7C, we can observe a relatively constant Vs value down to ca. 60 m depth followed by a section with a relatively stronger increase of Vs between 60- and 100-m depth. Beneath this section, we again have a depth range with relatively constant Vs values (between 100- and 150-m depth, Fig. 7C).

From the Bayesian inversion routine, we can also derive the interface probability function (Fig. 7D). This function shows the likelihood of layer interfaces inferred from the models generated during the inversion process. The resulting interface probability function close to the borehole location shows an interesting correlation with the magnetic susceptibility log (Fig. 7E), where we observe a clear change from lower magnetic susceptibility above a 42-m depth to higher values below this boundary. The interface probability function also indicates a relatively high probability of an interface at this depth (horizontal black, red, and magenta lines in Fig. 7C–E).

We inverted the HVSR data at all 87 station locations and compiled a 2D model by interpolation. We first defined a grid with 1×1 meter horizontal and vertical resolution. Missing Vs values between the station locations were then filled using linear interpolation. The model was then smoothed using a 2D moving average with a 2-m vertical window and 10-m horizontal window. We used a 12-m horizontal smoothing window using a running mean method to cover at least two stations worth of data. The resulting 2D Vs model is shown in Fig. 8. The bottom part of the model was cut off due to the expected low resolution, where the model is mainly defined by the modelled half space. In general, the Vs profile shows values between 0.85 and 2.50 km/s. Lateral variations are imaged primarily in the shallower regions down to ca. 40 m depth. Here, higher velocities are observed in the eastern part of the model, at distances between 0 and 120 m, where topography reaches the highest elevation along the profile. Below 40 m depth, we can see variations in the profile's eastern part (< 120 m profile distance) with higher Vs

Fig. 6. Synthetic model recovery test of a smooth Vs model using 24 chains, each with 100,000 iterations. (A) Synthetic HVSR curve (orange) and the noise-contaminated synthetic (blue) along the modelled curve from the inversion result (green). (B) Vs - depth model space with the model density heatmap. The true model is in red, and the recovered model is in blue. (C) Modelled and recovered Vs model. (D) Interface probability function from the inversion. (For interpretation of the references to colour in this figure legend, the reader is referred to the web version of this article.)

Fig. 7. Inversion result of the station located closest to the borehole location. (A) Observed and modelled HVSR curve from the Bayesian inversion, (B) 1D Vs probability density function from the generated models, (C) mean 1D Vs profile from HVSR inversion, (D) Interface probability density function, and (E) magnetic susceptibility log from the borehole data.
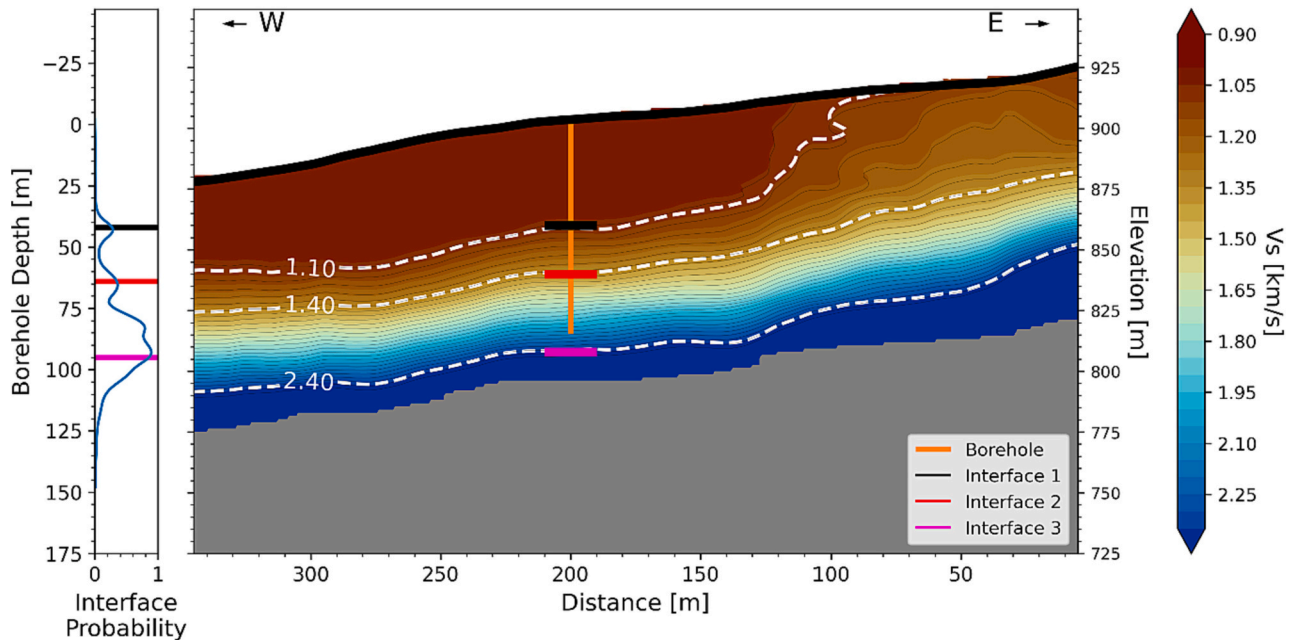
Fig. 8. The pseudo-2D Vs model was produced by interpolating 87 1D Vs models from the inversion of HVSR curves of each station location. The vertical orange line indicates the borehole, and the dashed white lines are contour lines whose values are chosen from the Vs value corresponding to the interface probability function at the borehole location (left panel). The thick black line on top of the model is the surface topography.

reaching upwards to the surface.

Vertically, we can observe three main velocity sections along the profile. The first section is the relatively constant velocity layer down to ca. 40–50 m depth with seismic velocity up to 1.1 km/s (Fig. 8, above interface 1). This section is also characterised by a relatively constant velocity value from the surface, which only increases from 0.85 km/s at the surface to 1.10 km/s at 40 m depth. Underlying this section of relatively low velocity, down to 80 m depth, we observe a section with a relatively high increase of seismic velocity. This section starts with a seismic velocity of around 1.10 km/s at 50 m depth to 2.40 km/s at 95 m depth (Fig. 8, between interfaces 1 and 3). This means the seismic velocity doubles in <50 m layer thickness. Following the section with a significant velocity increase, a third section starts from 2.40 km/s at 95

m depth. While we have not been able to resolve this depth, the seismic velocity value of this section appears to be relatively constant.

From the Vs model (Fig. 8), we can also calculate the vertical velocity gradient model (Fig. 9) that reveals how fast Vs is changing in vertical direction. This can indicate heterogeneities of the rock's physical properties (e.g., Bauer et al., 2010; Trichandi et al., 2022). A higher vertical velocity gradient value can be related to more rapid changes in rock properties, while a lower value means the rocks are relatively homogenous.

The upper 40 m in the vertical velocity gradient model (Fig. 9) show a relatively low vertical velocity gradient value, meaning no significant heterogeneity exists in this depth range. This is especially visible at profile distances >100 m (Fig. 9). In contrast, the medium to high
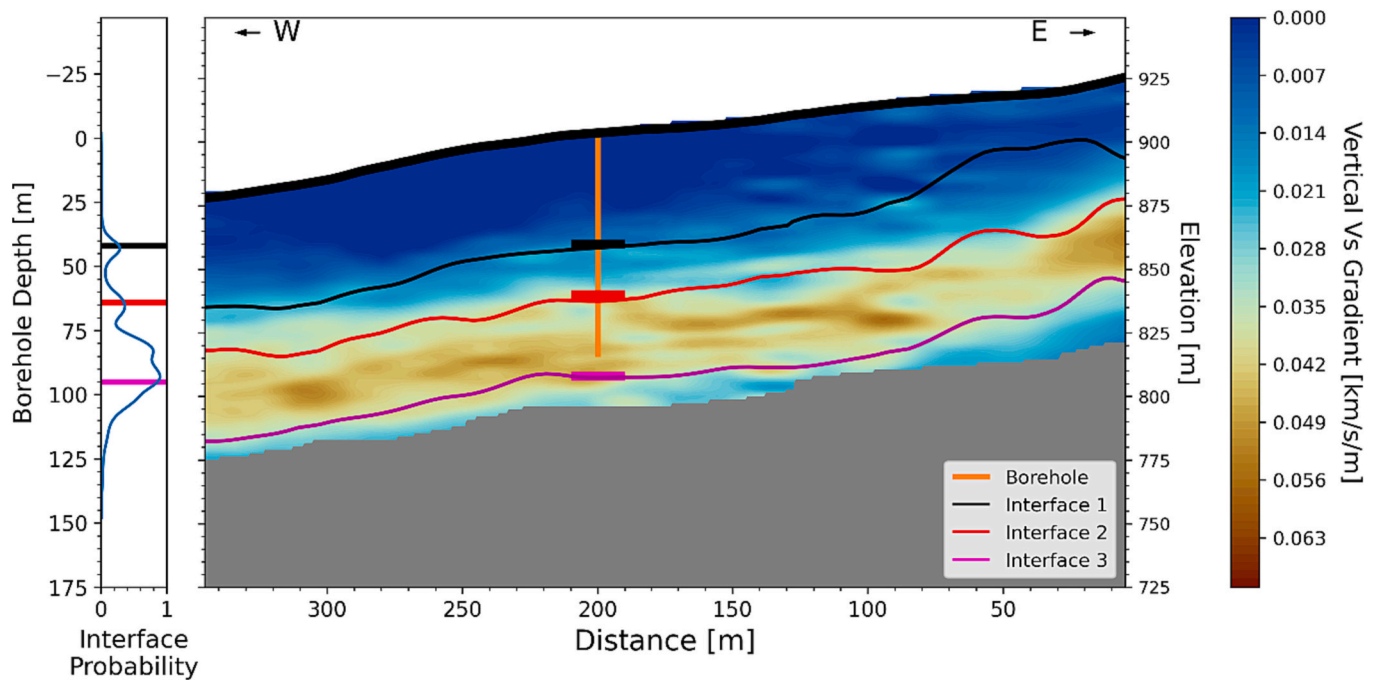
Fig. 9. Vertical Vs gradient model calculated from the Vs model (Fig. 8). Solid lines (black, red, and magenta) correspond to the manually picked peaks of the interface probability function from each station's HVSR curve inversion. The vertical orange line indicates the borehole location and depth. The corresponding interface probability function is shown as an example on the leftmost panel. (For interpretation of the references to colour in this figure legend, the reader is referred to the web version of this article.)

vertical velocity gradient between 40 and 95 m depth indicates that the rock properties change rapidly in this depth range. In the deeper part (> 95 m), although limited by the resolution, we again encounter a low vertical gradient value, suggesting no significant heterogeneity exists in this depth range.

In addition to the presented vertical velocity gradient model, we also present the manually picked interface from the individual interface probability function along the profile. The picking was done for each interface probability function from each station's result, similar to the interface we defined after inversion (Fig. 7D). The superimposed interface function in Fig. 9 shows that interface 2 (red line) and interface 3 (blue line) correspond nicely with the high vertical velocity gradient section along the profile. Additionally, an interesting feature is how the interface lines in the topographic high direction (eastern part of the profile) have more undulation and are getting more proximate to the surface compared to the lines located in the lower slope.

6. Discussion

The micro-tremor HVSR analysis and inversion using the Bayesian McMC inversion approach allows us to derive the absolute Vs, vertical velocity gradient, and interface probability models. These models provide us with three different perspectives on the weathering zone structure of the seismic profile in La Campana. We first discuss how the Bayesian inversion provides us with an edge on weathering front investigation using the HVSR method compared to other inversion techniques (subchapter 6.1). Then, we interpret the different identified layers along the profile with their different seismic characteristics (subchapter 6.2–6.5). Finally, we will discuss the possible process that could affect the weathering structure in the study area (subchapter 6.6).

6.1. Bayesian inversion application

One of the major advantages of using the Bayesian McMC approach to solve the inverse problem is that no initial information about the subsurface is required. Previous inversion approaches to the HVSR curve

include the least-square approach (Arai and Tokimatsu, 2004) and the genetic algorithm (Parolai et al., 2005). These approaches require multiple prior information such as the bedrock depth and velocity, number of layers, or even starting 1D Vs model (Moon et al., 2019; Nelson and McBride, 2019; Pilz et al., 2010) to constrain the inversion process. The usage of Bayesian McMC inversion, however, is relatively new, with only a few applications (Hallo et al., 2021). Using a Bayesian inversion, we can solve the inverse problem with a mostly unbiased, data-driven approach by providing only minimum prior information about the subsurface model (e.g., defining a wide range of parameter windows).

Bayesian inversion provides a relatively smooth subsurface model compared to the blocky 1D models from previously used inversion approaches (Moon et al., 2019; Nelson and McBride, 2019; Pilz et al., 2010). The smoothed model at La Campana (e.g., Fig. 8) provides more realistic information about the subsurface, especially in weathering front investigation, where the rock property changes are relatively gradual instead of sharp. The smooth model is also not a result of the smoothing of a block model but rather an average model inferred from all individual inversion results.

Another advantage of using the Bayesian approach is that the stochastic nature of the inversion process allows extensive exploration of the model space. Thus, the final inferred model could contain information from models that were already explored in previous iterations. Such a setting is especially pronounced with the first interface detected in La Campana (Fig. 7D), which corresponds to the increased magnetic susceptibility (Fig. 7E). Furthermore, the Bayesian inversion also provides us with data-driven information on potential interfaces based on the interface probability function produced from the inversion, which will be discussed for this investigation in the following layer-related subchapters.

6.2. Bedrock layer

We identified the top of the bedrock layer with a Vs value of 2.3 km/s, which we also interpret as the lower end of the weathering front.

Different Vs values can be used to define the boundaries between bedrock and overlying materials depending on the different lithologies, as shown in other similar studies in granitic rocks where 2.0 km/s were used as the top of the bedrock marker (Handoyo et al., 2022; Liu et al., 2022). A previous study in a similar granitic area in Santa Gracia National Park interprets a Vs value of 2.5 km/s as the lower end of the weathering zone (Trichandi et al., 2022). The chosen 2.3 km/s value, however, is also supported by the peak of the interface probability function at the borehole location (Fig. 7D, marked as the magenta line along Fig. 7C - E) as well as the limit of the high vertical velocity gradient (Fig. 9). Therefore, this discrepancy from the previous studies can be interpreted as lithological heterogeneities between the different sites or the differing climate that affects the site-specific weathering intensity.

In La Campana, the identified top of the bedrock layer is located around 75–100 m in depth, with the shallowest part located at the topographic high (Fig. 10). Previous studies on bedrock depth in different climates show that the depth of bedrock can range between a few to 10's meters depth. In a humid climate, bedrock is usually found between 10 and 20 m depth (e.g., Hayes et al., 2020), while in semi-arid and arid climates, bedrock depths can reach between 30 and 70 m (Stierman and Healy, 1984; Vázquez et al., 2016). Since the study site is located in a Mediterranean climate, we initially expected the bedrock's depth to be similar. However, seismically, we observe a greater depth to the top of the bedrock.

Another interesting feature that can be identified is the shallowing of the bedrock layer at the topographic high. The top of the bedrock layer is relatively parallel to the surface topography but becomes shallower in the eastern part of the profile around the topographic high (Fig. 10). This feature differs from hillslope predictions from combined water flow and erosion models (Rempe and Dietrich, 2014). In these models, the weathering zone is predicted to be highest at topographic highs. However, our site is located on a ridge, and the profiles were taken along the

ridge crest, perpendicular to these ridges to valley models. A similar feature was also observed, albeit on a different scale and location, in the Vs model along the Santiago de Chile basin, derived from the HVSR method (Pilz et al., 2010). Additionally, the seismic model in Santa Gracia National Park also observed this feature of shallowing bedrock around the topographic high (Trichandi et al., 2022).

6.3. Fractured bedrock layer

We associate the top of the fractured bedrock layer with the onset of the steep increase of Vs values (Fig. 10). The observed steep increase starts with a Vs value of 1.4 km/s to the top of the bedrock with a Vs value of 2.4 km/s. The 1.4 km/s Vs value for the top of the fractured bedrock layer is also supported by interface 2 (Fig. 9), while the Vs value of 2.4 km/s also correlates with interface 3. We identified a relatively similar Vs value compared to the interpreted boundary of 1.36 km/s in Santa Gracia National Park (Trichandi et al., 2022). This shows that the interface derived from the interface probability can yield a complementing data-driven approach instead of arbitrarily choosing a Vs value as a proxy for layer interfaces.

We identified the fractured bedrock layer in La Campana to be around 30 m thick. This is relatively thicker (~50%) than the identified fractured bedrock layer, with a thickness of approximately 20 m in Santa Gracia National Park (Trichandi et al., 2022). The thickness is also similar to the thickness of weathered or fractured bedrock identified in Pennsylvania (Liu et al., 2022) using both P- and S-wave tomography. This layer shows a relatively constant thickness along the whole profile. However, like the bedrock layer, the fractured bedrock layer reaches closer to the surface around the topographic high (Fig. 10). Since the top of the fractured bedrock and the top of the bedrock layer appear to run in parallel to topography, we expect that the extent of the top of the fractured bedrock layer is controlled more by surface inputs, meaning either weathering or fracturing driven by erosion (Eppes et al., 2018).
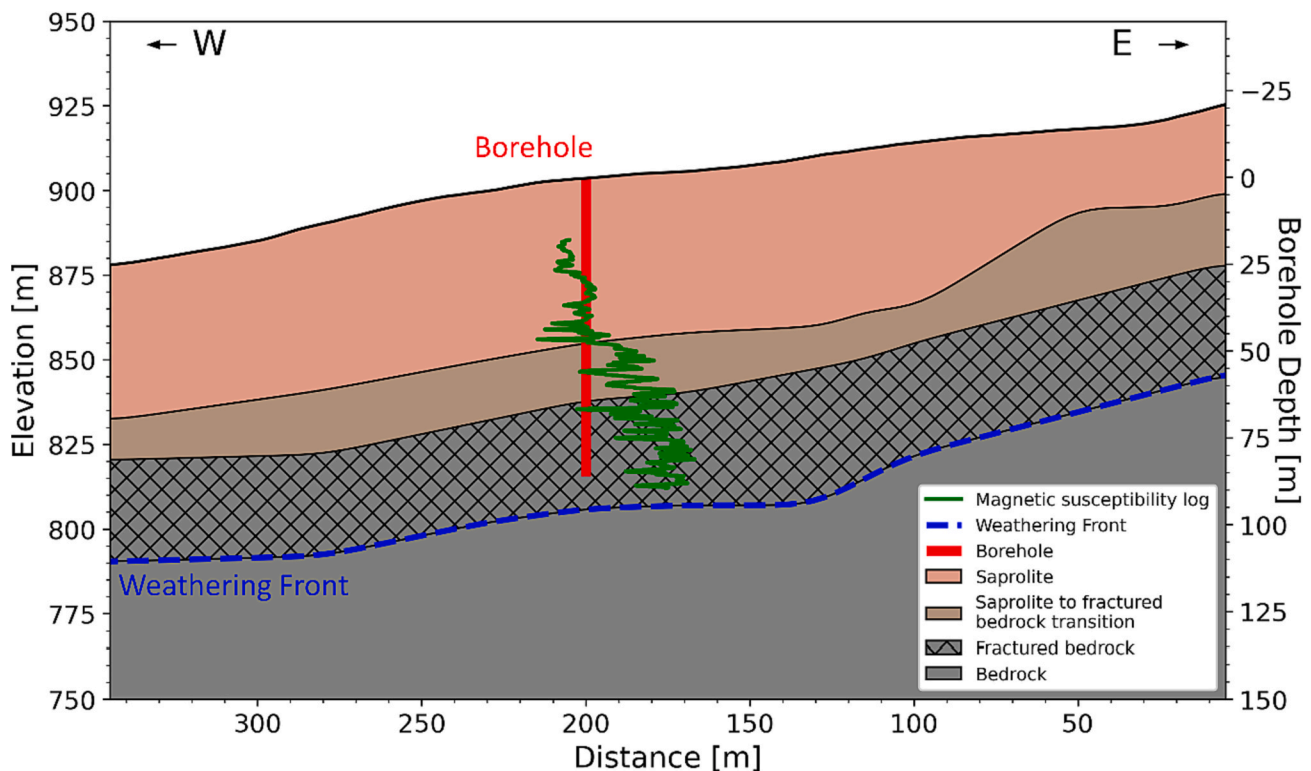

Fig. 10. The subsurface conceptual model along the seismic profile is based on Vs, Vs gradient, interface probability, and borehole data. The vertical red line represents the borehole location and depth extent, while the green line represents the borehole magnetic susceptibility log. The interpreted weathering front is shown as the dashed blue line. (For interpretation of the references to colour in this figure legend, the reader is referred to the web version of this article.)

The high vertical velocity gradient value indicates high heterogeneity in the fractured bedrock layer (Fig. 9). Based on the comparison between borehole information (rock porosity, Fe(III)/Fe ratio) and vertical variations in seismic velocity, Trichandi et al. (2022) interpreted two domains within the fractured bedrock in Santa Gracia National Park: an upper layer dominated by chemical weathering due to water infiltration, and a lower layer with more physically fractured bedrock. We propose a similar vertical zonation at La Campana. We hypothesise that such vertical zonation follows the distribution of open spaces in the rocks (e.g., porosity and fracture). In the upper part of the fractured bedrock, a high density of open fractures facilitates the infiltration of meteoric fluids and, consequently, the occurrence of chemical weathering. Several topographic stress models also show that the density of open fractures below a certain depth should decrease significantly (e.g., St. Clair et al., 2015; Riebe et al., 2017). A decrease in open fracture density can then be one limiting factor in precluding the circulation of fluids and the intensity of chemical weathering at depth. Nevertheless, the existence of open fracture does not always enable chemical weathering, as the saturation of the infiltrating fluids also controls the weathering processes. Therefore, the depth of the fractured bedrock is likely to vary along different sites depending on the local climate and differing tectonic processes.

We also identified a buffer zone that serves as the transition layer between the fractured bedrock and the saprolite layer. We seismically identified this layer with Vs between 1.1 and 1.4 km/s. The 1.1 km/s value was chosen as we identified a possible layer interface (interface 1 in Fig. 9) that also coincides with the changes in the magnetic susceptibility log (Fig. 7E). We speculate that we have a pronounced transition from the fractured bedrock to the saprolite layer in this layer, where more chemical weathering occurs.

6.4. Saprolite layer

Finally, we interpret the layer with Vs smaller than 1.10 km/s as the saprolite layer. Interpretation of the saprolite layer is also supported by the core analysis where the base of the saprolite is interpreted around 42 m depth, which correlates to Vs value of 1.05 km/s (Fig. 8). The saprolite layer is also characterised by the relatively constant Vs value with a relatively low vertical velocity gradient. The lowest Vs value of the saprolite is around 0.85 km/s, located at the surface. This is considerably higher than the 0.60 km/s saprolite Vs value found in Santa Gracia National Park (Trichandi et al., 2022). The varying degrees of weathering between the two sites can explain the absence of lower Vs along the seismic profile. In this case, with a higher Vs value in La Campana, one might speculate that the weathering degree in La Campana is lower compared to Santa Gracia. Indeed, while the weathering degree (as quantified by the chemical depletion fraction CDF) is ca. 0.35 at Santa Gracia (Krone et al., 2021), new data from the drill site at La Campana shows a CDF of ca. 0.2. The difference between these CDF values are likely too close to explain the difference in Vs. As the bedrock average Vs value in La Campana is larger than in Santa Gracia (2.3 and 2.5 km/s, respectively; Fig. 8), another explanation could be related to different bedrock lithology between the two sites. While the La Campana site exhibits mostly granodiorites (Molina et al., 2015; Oeser et al., 2018), bedrock in Santa Gracia has a more mafic composition, mainly diorites (Emparan and Pineda, 2000; Oeser et al., 2018). As granodiorites contain larger amounts of quartz and feldspar, the bedrock mineralogy in La Campana should be more resistant to weathering than in Santa Gracia, at least considering the original composition of bedrock and the lower CDF value between the two sites.

Along the seismic profile, the thickness of the saprolite layer varies between 42 and to 69-m. We also observed a similar thinning pattern of the saprolite layer in the topographic highs as we observed in the fractured bedrock and bedrock layers. This pattern also agrees with the observation in Santa Gracia National Park, where we observe thinner saprolite in topographic highs compared to the topographic lows

(Trichandi et al., 2022). However, the saprolite layer is much thicker in La Campana, whereas in Santa Gracia, we observe a saprolite layer with a maximum thickness of 15 m in the topographic low.

6.5. Saprolite – fractured bedrock transition

We define the transition from saprolite to fractured bedrock layer based on the interface probability function and magnetic susceptibility log available at the borehole location. A high interface probability value is found at a depth of around 42 m (Fig. 7D and Fig. 8), coinciding with the jump in the magnetic susceptibility log (Fig. 7E) and a Vs of 1.10 km/s. The Vs contour associated with this value line begins to rise at the 120-m profile distance and is closer to the surface near the topographic high at 75 m profile distance (Fig. 8). We interpret this layer between the 1.1 km/s and 1.4 km/s as a transitional layer between the saprolite and fractured bedrock where effects of surface-related weathering processes such as water infiltration and chemical alteration quickly change. However, this weathering effect can still affect parts of the underlying fractured bedrock layer, thus the identified buffer zone in the fractured bedrock layer. Lower magnetic susceptibility values at shallow depths can be explained by the alteration of magnetite caused by meteoric water (e.g., Clark, 2014), where infiltration is facilitated by higher porosity (within the saprolite) or open fractures (within the transition from saprolite to fractured bedrock). It is also possible that instead of alterations of magnetite, the infiltrating water removes the magnetite from this layer and thus reduces the magnetite concentration. However, it cannot be discarded that this change in magnetic susceptibility may also be influenced, at least partially, by hydrothermal alteration processes preceding weathering. For instance, Hampl et al. (2022) suggest that changes in magnetic susceptibility observed in Santa Gracia are attributed to magnetite alteration due to hydrothermal processes rather than weathering.

6.6. Controlling processes

Different approaches can generally explain subsurface weathering structure and weathering front advance. A 'bottom-up' advancement of the weathering front is primarily controlled by surface topography and groundwater level (Rempe and Dietrich, 2014). However, the absence of an observed groundwater table in the study site makes it less likely that a 'bottom-up' approach can explain the advancement of the weathering front.

With the absence of a groundwater table in La Campana, the 'top-down' control of weathering front advancement is the preferred controlling process. 'Top-down' control of the weathering front suggests that the advance of the weathering front is mainly controlled by the infiltration of oxygen and meteoric water into the bedrock (Brantley and White, 2009). The oxygen is brought from the atmosphere to depth along fractures and connected pores. Its effect is that the iron(II) in minerals like biotite is partially oxidised to iron(III). This transformation entails a volume increase, which produces "weathering-induced fractures" (Behrens et al., 2021; Goodfellow et al., 2016; Navarre-Sitchler et al., 2015). The meteoric water is provided by precipitation and infiltrates the subsurface, which induces chemical weathering at depth. At La Campana, expandable clays are formed, which also increases mineral volume (Hampl et al., 2022). Both processes, clay formation and Fe(II) oxidation, lead to weathering-induced fracturing at depth. Thus, positive feedback is induced where water infiltration and oxygen transport increase the hydraulic conductivity. Further water can then be transported from the surface to the subsurface (Hampl et al., 2022). Assuming identical rock properties, the resulting weathering structure should be similar along the profile. However, this is not what we observe in the Vs model (Fig. 8), where we observe horizontal variations of the weathering structure. This indicates possibly different rock properties along the seismic profile. Differences in fracture density are a likely explanation because higher fracture density enables even more water

infiltration and transport of oxygen to depth (Andrews et al., 2023; St. Clair et al., 2015).

7. Conclusion and outlook

The study in La Campana showcases the potential of the passive seismic method in imaging weathering structures such as regolith. With passive seismic methods, we eliminate the requirement of the active seismic source, which can often be hard to transport or is not allowed in a conservation area. Since data processing is done for each station location separately, it also simplifies the acquisition setup compared to the active seismic method, where a straight line is often preferred.

We also demonstrate data quality improvement of the HVSR curve by performing temporal analysis of the HVSR curve standard deviation. The presented processing steps can help the future application of the HVSR method in selecting the optimum data window for the HVSR analysis. As for the inversion step, applying the hierarchical Bayesian McMC approach allows us to reconstruct the 1D Vs model using the HVSR curve with minimum prior information. This is helpful when no information on the subsurface structure is available and thus enables the application of HVSR imaging as the preliminary survey method in subsurface imaging or exploration. Additionally, the interface probability function yields data-driven information on the layer interpretation of the weathering structure.

The seismically identified weathering front in La Campana reaches down to 110 m depth. The depth of the weathering front is significantly deeper when compared to similar studies on granitic bodies in Chile and is related to the higher precipitation rate, which enhances the 'top-down' weathering process. Bedrock pre-conditioning and surface topography are important parameters controlling the weathering front depth. These findings and methodical approaches are accessible now to further investigate the coupling between landscape topography and bedrock weathering in general.

CRediT authorship contribution statement

Rahmantara Trichandi: Writing – review & editing, Writing – original draft, Visualization, Validation, Software, Resources, Methodology, Investigation, Formal analysis, Data curation, Conceptualization. **Klaus Bauer:** Writing – review & editing, Writing – original draft, Validation, Supervision, Software, Project administration, Methodology, Investigation, Funding acquisition, Conceptualization. **Trond Ryberg:** Writing – review & editing, Visualization, Validation, Software, Resources, Methodology. **Britta Wawerzinek:** Writing – review & editing, Visualization, Validation, Resources, Investigation, Data curation. **Jaime Araya Vargas:** Writing – review & editing, Visualization, Resources, Investigation. **Friedhelm von Blankenburg:** Writing – review & editing, Supervision, Resources, Project administration, Investigation, Funding acquisition, Conceptualization. **Charlotte M. Krawczyk:** Writing – review & editing, Supervision, Resources, Project administration, Funding acquisition, Conceptualization.

Declaration of Competing Interest

Rahmantara Trichandi reports financial support was provided by German Research Foundation.

Data availability

The data that support the findings will be available in the GFZ Data Repository following an embargo to allow for doctoral publication of research findings.

Acknowledgments

Appendix A. Supplementary data

Supplementary data to this article can be found online at https://doi.org/10.1016/j.jappgeo.2023.105191.

References

Al-Halbouni, D., Watson, R.A., Holohan, E.P., Meyer, R., Polom, U., Dos Santos, F.M., Comas, X., Alrshdan, H., Krawczyk, C.M., Dahm, T., 2021. Dynamics of hydrological and geomorphological processes in evaporite karst at the eastern Dead Sea – a multidisciplinary study. Hydrol. Earth Syst. Sci. 25 (6), 3351–3395. https://doi.org/10.5194/hess-25-3351-2021.

Andrews, E.M., Hyman, J.D., Sweeney, M.R., Karra, S., Moulton, J.D., Navarre-Sitchler, A., 2023. Fracture intensity impacts on reaction front propagation and mineral weathering in three-dimensional fractured media. Water Resour. Res. 59 (2) https://doi.org/10.1029/2022WR032121.

Arai, H., Tokimatsu, K., 2004. S-wave velocity profiling by inversion of micro-tremor H/V spectrum. Bull. Seismol. Soc. Am. 94 (1).

Arai, H., Tokimatsu, K., 2005. S-wave velocity profiling by joint inversion of micro-tremor dispersion curve and horizontal-to-vertical (H/V) spectrum. Bull. Seismol. Soc. Am. 95 (5), 1766–1778. https://doi.org/10.1785/0120040243.

Arroyo, M.T.K., Armesto, J.J., Squeo, F., Gutierrez, J., 1993. Global change: Flora and vegetation of Chile. In: Earth System Responses to Global Change: Contrasts between North and South America, January, 239–263. http://books.google.com/books?hl=en&lr=&id=QgzEcsIZDYwC&oi=fnd&pg=PA239&dq=Global+Change:+Flora+and+Vegetation+of+Chile&ots=jZzaCGfgwB&sig=eCuLBzidmGQHGkrb-3CdKgVQ1nI.

Bauer, K., Moeck, I., Norden, B., Schulze, A., Weber, M., Wirth, H., 2010. Tomographic P wave velocity and vertical velocity gradient structure across the geothermal site Groß Schönebeck (NE German Basin): relationship to lithology, salt tectonics, and thermal regime. J. Geophys. Res. Solid Earth 115 (8), 1–22. https://doi.org/10.1029/2009JB006895.

Befus, K.M.M., Sheehan, A.F.F., Leopold, M., Anderson, S.P.P., Anderson, R.S.S., 2011. Seismic constraints on critical zone architecture, boulder creek watershed, Front Range, Colorado. Vadose Zone J. 10 (3), 915. https://doi.org/10.2136/vzj2010.0108.

Behrens, R., Wirth, R., von Blanckenburg, F., 2021. Rate limitations of nano-scale weathering front advance in the slow-eroding Sri Lankan Highlands. Geochim. Cosmochim. Acta 311, 174–197. https://doi.org/10.1016/j.gca.2021.06.003.

Bernhard, N., Moskwa, L.M., Schmidt, K., Oeser, R.A., Aburto, F., Bader, M.Y., Baumann, K., von Blanckenburg, F., Boy, J., van den Brink, L., Brucker, E., Büdel, B., Canessa, R., Dippold, M.A., Ehlers, T.A., Fuentes, J.P., Godoy, R., Jung, P., Karsten, U., Köster, M., Kuzyakov, Y., Leinweber, P., Neidhardt, H., Matus, F., Mueller, C.W., Oelmann, Y., Oses, R., Osses, P., Paulino, L., Samolov, E., Schaller, M., Schmid, M., Spielvogel, S., Spohn, M., Stock, S., Stroncik, N., Tielbörger, K., Übernickel, K., Scholten, T., Seguel, O., Wagner, D., Kühn, P., 2018. Pedogenic and microbial interrelations to regional climate and local topography: New insights from a climate gradient (arid to humid) along the Coastal Cordillera of Chile. Catena 170, 335–355. https://doi.org/10.1016/j.catena.2018.06.018.

Bodin, T., 2010. Transdimensional Approaches to Geophysical Inverse Problems. PhD Thesis, October, 243. https://doi.org/10.1021/jo00151a027.

Bodin, T., Sambridge, M., Tkalćić, H., Arroucau, P., Gallagher, K., Rawlinson, N., 2012. Transdimensional inversion of receiver functions and surface wave dispersion. J. Geophys. Res. Solid Earth 117 (2), 1–24. https://doi.org/10.1029/2011JB008560.

Bonnefoy-Claudet, S., Cotton, F., Bard, P.Y., 2006. The nature of noise wavefield and its applications for site effects studies. A literature review. Earth Sci. Rev. 79 (3–4), 205–227. https://doi.org/10.1016/j.earscirev.2006.07.004.

Brantley, S.L., White, A.F., 2009. Approaches to modeling weathered regolith. In: Thermodynamics and Kinetics of Water-Rock Interaction, pp. 435–484. De Gruyter. https://doi.org/10.1515/9781501508462-012.

Cipta, A., Cummins, P., Dettmer, J., Saygin, E., Irsyam, M., Rudyanto, A., Murjaya, J., 2018. Seismic velocity structure of the Jakarta Basin, Indonesia, using trans-dimensional Bayesian inversion of horizontal-to-vertical spectral ratios. Geophys. J. Int. 215 (1), 431–449. https://doi.org/10.1093/gji/ggy289.

Clark, D.A., 2014. Magnetic effects of hydrothermal alteration in porphyry copper and iron-oxide copper-gold systems: a review. Tectonophysics 624–625, 46–65. https://doi.org/10.1016/j.tecto.2013.12.011.

Cox, B.R., Cheng, T., Vantassel, J.P., Manuel, L., 2021. A statistical representation and frequency-domain window-rejection algorithm for single-station HVSR measurements. Geophys. J. Int. 221 (3), 2170–2183. https://doi.org/10.1093/GJI/GGAA119.

Cultrera, G., Cornou, C., Di Giulio, G., Bard, P.Y., 2021. Indicators for site characterization at seismic station: recommendation from a dedicated survey. Bull. Earthq. Eng. 19 (11), 4171–4195. https://doi.org/10.1007/s10518-021-01136-7.

Dal Bo, I., Klotzsche, A., Schaller, M., Ehlers, T.A., Kaufmann, M.S., Fuentes Espoz, J.P., Vereecken, H., van der Kruk, J., 2019. Geophysical imaging of regolith in landscapes along a climate and vegetation gradient in the Chilean coastal cordillera. Catena 180 (August 2018), 146–159. https://doi.org/10.1016/j.catena.2019.04.023.

Emparan, C., Pineda, G., 2000. Área La Serena – La Higuera, Región de Coquimbo. Servicio Nacional de Geología y Minería. Mapas Geológicos, n°18, 1 mapa escala 1: 100.000.

Eppes, M.C., Hancock, G.S., Chen, X., Arey, J., Dewers, T., Huettenmoser, J., Kiessling, S., Moser, F., Tannu, N., Weiserbs, B., Whitten, J., 2018. Rates of subcritical cracking and long-term rock erosion. Geology 46 (11), 951–954. https://doi.org/10.1130/G45256.1.

Fäh, D., Kind, F., Giardini, D., 2001. A theoretical investigation of average H/V ratios. Geophys. J. Int. 145 (2), 535–549. https://doi.org/10.1046/j.0956-540x.2001.01406.x.

Fäh, D., Kind, F., Giardini, D., 2003. Inversion of local S-wave velocity structures from average H/V ratios, and their use for the estimation of site-effects. J. Seismol. 7 (4), 449–467. https://doi.org/10.1023/B:JOSE.0000005712.86058.42.

Flinchum, B.A., Steven Holbrook, W., Rempe, D., Moon, S., Riebe, C.S., Carr, B.J., Hayes, J.L., Clair, J.S., Peters, M.P., 2018. Critical zone structure under a granite ridge inferred from drilling and three-dimensional seismic refraction data. J. Geophys. Res. Earth 123 (6), 1317–1343. https://doi.org/10.1029/2017JF004280.

Gana, P., Wall, R., Gutiérrez, A., 1996. Mapa geológico del area de Valparaiso-Curacavi, Regiones de Valparaiso y Metropolitanae.

Goodfellow, B.W., Hilley, G.E., Webb, S.M., Sklar, L.S., Moon, S., Olson, C.A., 2016. The chemical, mechanical, and hydrological evolution of weathering granitoid. J. Geophys. Res. Earth 121 (8), 1410–1435. https://doi.org/10.1002/2016JF003822.

Hallo, M., Imperatori, W., Panzera, F., Fäh, D., 2021. Joint multizonal transdimensional Bayesian inversion of surface wave dispersion and ellipticity curves for local near-surface imaging. Geophys. J. Int. 226 (1), 627–659. https://doi.org/10.1093/gji/ggab116.

Hampl, F.J., Schiperski, F., Byrne, J.M., Schwerdhelm, C., Kappler, A., Bryce, C., von Blanckenburg, F., Neumann, T., 2022. The role of iron-bearing minerals for the deep weathering of a hydrothermally altered plutonic rock in semi-arid climate (Chilean Coastal Cordillera). Chem. Geol. 604 (November 2021) https://doi.org/10.1016/j.chemgeo.2022.120922.

Hampl, F.J., Schiperski, F., Schwerdhelm, C., Stroncik, N., Bryce, C., Von Blanckenburg, F., Neumann, T., 2023. Feedbacks between the formation of secondary minerals and the infiltration of fluids into the regolith of granitic rocks in different climatic zones (Chilean Coastal Cordillera). Earth Surf. Dyn. 11 (3), 511–528. https://doi.org/10.5194/esurf-11-511-2023.

Handoyo, H., Defelipe, I., Martín-Banda, R., García-Mayordomo, J., Martí, D., Martínez-Díaz, J.J., Insua-Arévalo, J.M., Teixidó, T., Alcalde, J., Palomeras, I., Carbonell, R., 2022. Characterization of the shallow subsurface structure across the Carrascoy Fault System (SE Iberian Peninsula) using P-wave tomography and Multichannel Analysis of Surface Waves. Geol. Acta 20 (9), 1–19. https://doi.org/10.1344/GeologicaActayear.volume.manuscript.

Hayes, N.R., Buss, H.L., Moore, O.W., Krám, P., Pancost, R.D., 2020. Controls on granitic weathering fronts in contrasting climates. Chem. Geol. 535, 119450. https://doi.org/10.1016/j.chemgeo.2019.119450.

Hobiger, M., Cornou, C., Wathelet, M., Di Giulio, G., Knapmeyer-Endrun, B., Renalier, F., Bard, P.Y., Savvaidis, A., Hailemikael, S., Le Bihan, N., Ohrnberger, M., Theodoulidis, N., 2013. Ground structure imaging by inversions of Rayleigh wave ellipticity: sensitivity analysis and application to European strong-motion sites. Geophys. J. Int. 192 (1), 207–229. https://doi.org/10.1093/gji/ggs005.

Holbrook, W.S., Riebe, C.S., Elwaseif, M., Hayes, J.L., Basler-Reeder, K., Harry, D.L., Malazian, A., Dosseto, A., Hartsough, P.C., Hopmans, J.W., 2014. Geophysical constraints on deep weathering and water storage potential in the Southern Sierra Critical Zone Observatory. Earth Surf. Process. Landf. 39 (3), 366–380. https://doi.org/10.1002/esp.3502.

Karger, D.N., Conrad, O., Böhner, J., Kawohl, T., Kreft, H., Soria-Auza, R.W., Zimmermann, N.E., Linder, H.P., Kessler, M., 2017. Climatologies at high resolution for the earth's land surface areas. Sci. Data 4, 1–20. https://doi.org/10.1038/sdata.2017.122.

Koesuma, S., Ridwan, M., Nugraha, A.D., Widiyantoro, S., Fukuda, Y., 2017. Preliminary estimation of engineering bedrock depths from micro-tremor array measurements in Solo, Central Java, Indonesia. J. Math. Fundam. Sci. 49 (3), 306–320. https://doi.org/10.5614/j.math.fund.sci.2017.49.3.8.

Krawczyk, C.M., Polom, U., Trabs, S., Dahm, T., 2012. Sinkholes in the city of Hamburg-New urban shear-wave reflection seismic system enables high-resolution imaging of subrosion structures. J. Appl. Geophys. 78, 133–143. https://doi.org/10.1016/j.jappgeo.2011.02.003.

Krone, L.V., Hampl, F.J., Schwerdhelm, C., Bryce, C., Ganzert, L., Kitte, A., Übernickel, K., Dielforder, A., Aldaz, S., Oses-Pedraza, R., Perez, J.P.H., Sanchez-Alfaro, P., Wagner, D., Weckmann, U., von Blanckenburg, F., 2021. Deep weathering in the semi-arid Coastal Cordillera, Chile. Scientific Reports 11, 13057. https://doi.org/10.1038/s41598-021-90267-7.

Lachet, C., Bard, P.Y., 1994. Numerical and Theoretical Investigations on the Possibilities and Limitations of Nakamura's Technique. J. Phys. Earth 42 (5), 377–397. https://doi.org/10.4294/jpe1952.42.377.

Lermo, J., Chávez-García, F.J., 1993. Site effect evaluation using spectral ratios with only one station. Bull. Seismol. Soc. Am. 83 (5), 1574–1594. https://doi.org/10.1785/BSSA0830051574.

Liu, X., Zhu, T., Hayes, J., 2022. Critical zone structure by elastic full waveform inversion of seismic refractions in a sandstone catchment, Central Pennsylvania, USA. J. Geophys. Res. Solid Earth 127 (3), 1–17. https://doi.org/10.1029/2021JB023321.

Longuet-Higgins, M.S., 1950. A theory of the origin of microseisms. Philos. Trans. R. Soc. Lond. Ser. A Math. Phys. Sci. 243 (857), 1–35. https://doi.org/10.1098/rsta.1950.0012.

Lontsi, A.M., Sánchez-Sesma, F.J., Molina-Villegas, J.C., Ohrnberger, M., Krüger, F., 2015. Full micro-tremor H/V(z,f) inversion for shallow subsurface characterization. Geophys. J. Int. 202 (1), 298–312. https://doi.org/10.1093/gji/ggv132.

Lontsi, A.M., Hobiger, M., Panzera, F., Sánchez-Sesma, F.J., Fäh, D., 2023. Seismic characterization of swiss strong-motion borehole-station sites by inversion of full micro-tremor horizontal-to-vertical spectral ratios [H/V(z,f)]. Bull. Seismol. Soc. Am. 113 (1), 417–436. https://doi.org/10.1785/0120210320.

Maghami, S., Sohrabi-Bidar, A., Bignardi, S., Zarean, A., Kamalian, M., 2021. Extracting the shear wave velocity structure of deep alluviums of "Qom" Basin (Iran) employing HVSR inversion of micro-tremor recordings. J. Appl. Geophys. 185, 104246. https://doi.org/10.1016/j.jappgeo.2020.104246.

Mahajan, A.K., Mundepi, A.K., Chauhan, N., Jasrotia, A.S., Rai, N., Gachhayat, T.K., 2012. Active seismic and passive micro-tremor HVSR for assessing site effects in Jammu city, NW Himalaya, India – a case study. J. Appl. Geophys. 77, 51–62. https://doi.org/10.1016/j.jappgeo.2011.11.005.

Molina, P.G., Parada, M.A., Gutiérrez, F.J., Ma, C., Li, J., Yuanyuan, L., Reich, M., Aravena, Á., 2015. Protracted late magmatic stage of the Caleu pluton (Central Chile) as a consequence of heat redistribution by diking: Insights from zircon data and thermal modeling. Lithos 227, 255–268. https://doi.org/10.1016/j.lithos.2015.04.008.

Moon, S.W., Subramaniam, P., Zhang, Y., Vinoth, G., Ku, T., 2019. Bedrock depth evaluation using micro-tremor measurement: empirical guidelines at weathered granite formation in Singapore. J. Appl. Geophys. 171, 103866. https://doi.org/10.1016/j.jappgeo.2019.103866.

Mucciarelli, M., Gallipoli, M.R., 2001. A critical review of 10 years of micro-tremor HVSR technique. Boll. Geofis. Teor. Appl. 42 (3–4), 255–266.

Nardone, L., Vassallo, M., Cultrera, G., Sapia, V., Petrosino, S., Pischiutta, M., Di Vito, M., de Vita, S., Galluzzo, D., Milana, G., Bellucci Sessa, E., Bobbio, A., Bordoni, P., Cara, F., Carandente, A., Civico, R., Cogliano, R., Cusano, P., Di Giulio, G., Esposito, R., Famiani, D., Fodarella, A., Giannattasio, F., Marchetti, M., Marotta, E., Moretti, M., Napolitano, F., Pucillo, S., Riccio, G., Sepe, V., Tarabusi, G., Tramelli, A., 2023. A geophysical multidisciplinary approach to investigate the shallow subsoil structures in volcanic environment: the case of Ischia Island. J. Volcanol. Geotherm. Res. 438, 107820. https://doi.org/10.1016/j.jvolgeores.2023.107820.

Navarre-Sitchler, A., Brantley, S.L., Rother, G., 2015. How porosity increases during incipient weathering of crystalline silicate rocks. Pore Scale Geochem. Process. 80 (Tugrul 2004), 331–354. https://doi.org/10.2138/rmg.2015.80.10.

Nelson, S., McBride, J., 2019. Application of HVSR to estimating thickness of laterite weathering profiles in basalt. Earth Surf. Process. Landf. 44 (7), 1365–1376. https://doi.org/10.1002/esp.4580.

Oeser, R.A., Von Blanckenburg, F., 2020. Do degree and rate of silicate weathering depend on plant productivity? Biogeosciences 17 (19), 4883–4917. https://doi.org/10.5194/bg-17-4883-2020.

Oeser, R.A., Stroncik, N., Moskwa, L.M., Bernhard, N., Schaller, M., Canessa, R., van den Brink, L., Köster, M., Brucker, E., Stock, S., Fuentes, J.P., Godoy, R., Matus, F.J., Oses Pedraza, R., Osses McIntyre, P., Paulino, L., Seguel, O., Bader, M.Y., Boy, J., Dippold, M.A., Ehlers, T.A., Kühn, P., Kuzyakov, Y., Leinweber, P., Scholten, T., Spielvogel, S., Spohn, M., Übernickel, K., Tielbörger, K., Wagner, D., von Blanckenburg, F., 2018. Chemistry and microbiology of the Critical Zone along a steep climate and vegetation gradient in the Chilean Coastal Cordillera. Catena 170 (December 2017), 183–203. https://doi.org/10.1016/j.catena.2018.06.002.

Olona, J., Pulgar, J.A., Fernández-Viejo, G., López-Fernández, C., González-Cortina, J.M., 2010. Weathering variations in a granitic massif and related geotechnical properties through seismic and electrical resistivity methods. Near Surface Geophys. 8 (6), 585–599. https://doi.org/10.3997/1873-0604.2010043.

Parada, M.A., Roperch, P., Guiresse, C., Ramírez, E., 2005. Magnetic fabrics and compositional evidence for the construction of the Caleu pluton by multiple injections, Coastal Range of Central Chile. Tectonophysics 399, 399–420. https://doi.org/10.1016/j.tecto.2004.12.032, 1-4 SPEC. ISS.

Parolai, S., Picozzi, M., Richwalski, S.M., Milkereit, C., 2005. Joint inversion of phase velocity dispersion and H/V ratio curves from seismic noise recordings using a genetic algorithm, considering higher modes. Geophys. Res. Lett. 32 (1), 1–4. https://doi.org/10.1029/2004GL021115.

Pastén, C., Sáez, M., Ruiz, S., Leyton, F., Salomón, J., Poli, P., 2016. Deep characterization of the Santiago Basin using HVSR and cross-correlation of ambient seismic noise. Eng. Geol. 201, 57–66. https://doi.org/10.1016/j.enggeo.2015.12.021.

Pilz, M., Parolai, S., Picozzi, M., Wang, R., Leyton, F., Campos, J., Zschau, J., 2010. Shear wave velocity model of the Santiago de Chile basin derived from ambient noise measurements: a comparison of proxies for seismic site conditions and amplification. Geophys. J. Int. 182 (1), 355–367. https://doi.org/10.1111/j.1365-246X.2010.04613.x.

Piña-Flores, J., Cárdenas-Soto, M., García-Jerez, A., Seivane, H., Luzón, F., Sánchez-Sesma, F.J., 2020. Use of peaks and troughs in the horizontal-to-vertical spectral

ratio of ambient noise for Rayleigh-wave dispersion curve picking. J. Appl. Geophys. 177, 104024. https://doi.org/10.1016/j.jappgeo.2020.104024.

Rempe, D.M., Dietrich, W.E., 2014. A bottom-up control on fresh-bedrock topography under landscapes. Proc. Natl. Acad. Sci. U. S. A. 111 (18), 6576–6581. https://doi.org/10.1073/pnas.1404763111.

Riebe, C.S., Hahm, W.J., Brantley, S.L., 2017. Controls on deep critical zone architecture: a historical review and four testable hypotheses. Earth Surf. Process. Landf. 42 (1), 128–156. https://doi.org/10.1002/esp.4052.

Ryberg, T., Haberland, C., 2019. Bayesian simultaneous inversion for local earthquake hypocentres and 1-D velocity structure using minimum prior knowledge. Geophys. J. Int. 218 (2), 840–854. https://doi.org/10.1093/gji/ggz177.

Scherbaum, F., Hinzen, K.G., Ohrnberger, M., 2003. Determination of shallow shear wave velocity profiles in the cologne, Germany area using ambient vibrations. Geophys. J. Int. 152 (3), 597–612. https://doi.org/10.1046/j.1365-246X.2003.01856.x.

SESAME, 2004. Guidelines for the Implementation of the H/V Spectral Ratio Technique on Ambient Vibrations-Measurements, Processing and Interpretations, SESAME European Research Project. SESAME: Site EffectS Assessment Using Ambient Excitations, pp. 1–62. March.

Spica, Z.J., Perton, M., Nakata, N., Liu, X., Beroza, G.C., 2018. Site characterization at Groningen gas field area through joint surface-borehole H/V analysis. Geophys. J. Int. 212 (1), 412–421. https://doi.org/10.1093/gji/ggx426.

St. Clair, J., Moon, S., Holbrook, W.S., Perron, J.T., Riebe, C.S., Martel, S.J., Carr, B., Harman, C., Singha, K., De Richter, D.B., 2015. Geophysical imaging reveals topographic stress control of bedrock weathering. Science 350 (6260), 534–538. https://doi.org/10.1126/science.aab2210.

Stephenson, W.R., February 2003. Factors bounding prograde Rayleigh-wave particle motion in a soft-soil layer. In: Proceedings of the 2003 Pacific Conference on Earthquake Engineering. New Zealand Society of Earthquake Engineering, Christchurch, New Zealand, pp. 13–15.

Stierman, D.J., Healy, J.H., 1984. A study of the depth of weathering and its relationship to the mechanical properties of near-surface rocks in the Mojave Desert. Pure Appl. Geophys. PAGEOPH 122 (2–4), 425–439. https://doi.org/10.1007/BF00874609.

Trichandi, R., Bauer, K., Ryberg, T., Scherler, D., Bataille, K., Krawczyk, C.M., 2022. Combined seismic and borehole investigation of the deep granite weathering structure—Santa Gracia Reserve case in Chile. Earth Surf. Process. Landf. 1–15. https://doi.org/10.1002/esp.5457. June.

Vantassel, J., 2020. *hvsrpy* (latest (Concept)). Zenodo. https://doi.org/10.5281/zenodo.3666956.

Vázquez, M., Ramírez, S., Morata, D., Reich, M., Braun, J.J., Carretier, S., 2016. Regolith production and chemical weathering of granitic rocks in Central Chile. Chem. Geol. 446, 87–98. https://doi.org/10.1016/j.chemgeo.2016.09.023.

Wadas, S.H., Tschache, S., Polom, U., Krawczyk, C.M., 2020. Ground instability of sinkhole areas indicated by elastic moduli and seismic attributes. Geophys. J. Int. 222 (1), 289–304. https://doi.org/10.1093/gji/ggaa167.

Wathelet, M., Jongmans, D., Ohrnberger, M., 2004. Surface-wave inversion using a direct search algorithm and its application to ambient vibration measurements. Near Surface Geophys. 2 (4), 211–221. https://doi.org/10.3997/1873-0604.2004018.

Wathelet, M., Chatelain, J.L., Cornou, C., Di Giulio, G., Guillier, B., Ohrnberger, M., Savvaidis, A., 2020. Geopsy: a user-friendly open-source tool set for ambient vibration processing. Seismol. Res. Lett. https://doi.org/10.1785/0220190360.

Yamanaka, H., Dravinski, M., Kagami, H., 1993. Continuous measurements of microtremors on sediments and basement in Los Angeles, California. Bull. Seismol. Soc. Am. 83 (5), 1595–1609. https://doi.org/10.1785/BSSA0830051595.